



HAL
open science

Slippery flows of a Carbopol gel in a microchannel

Eliane Younes, Cathy Castelain, Teodor Burghelea, Volfango Bertola

► **To cite this version:**

Eliane Younes, Cathy Castelain, Teodor Burghelea, Volfango Bertola. Slippery flows of a Carbopol gel in a microchannel. *Physical Review Fluids*, 2020, 5 (8), 10.1103/PhysRevFluids.5.083303. hal-02970815

HAL Id: hal-02970815

<https://hal.science/hal-02970815>

Submitted on 25 Nov 2020

HAL is a multi-disciplinary open access archive for the deposit and dissemination of scientific research documents, whether they are published or not. The documents may come from teaching and research institutions in France or abroad, or from public or private research centers.

L'archive ouverte pluridisciplinaire **HAL**, est destinée au dépôt et à la diffusion de documents scientifiques de niveau recherche, publiés ou non, émanant des établissements d'enseignement et de recherche français ou étrangers, des laboratoires publics ou privés.

Slippery flows of a Carbopol gel in a micro-channel

Eliane Younes,^{*} Cathy Castelain,[†] and Teodor Burghelca[‡]

Université de Nantes, CNRS, Laboratoire de thermique et énergie de Nantes, LTeN, F-44000 Nantes, France

Volfango Bertola[§]

*Laboratory of Technical Physics, School of Engineering,
University of Liverpool, Liverpool, L69 3GH, United Kingdom*

(Dated: November 25, 2020)

The ability to predict and/or control wall slip is a fundamental problem in the hydrodynamics of yield stress fluids, which is poorly understood to date and has important applications in bio- and micro-fluidic systems. Systematic measurements of steady flows of a simple yield stress fluid (Carbopol Ultrez 10) in a plane acrylic micro-channel are used to establish rigorous scaling laws for the wall velocity gradient and the slip velocity. By means of epi-fluorescent microscopy combined with a custom developed Digital Particle Image Velocimetry (DPIV) technique, times series of velocity fields were measured within a wide range of flow rates and three distinct flow regimes were identified: full plug, partial plug and fully yielded. Corresponding to each flow regime, wall velocity gradients and slip velocities were obtained by extrapolating the velocity profiles using a smoothing spline function. By combining the flow field measurements with the macro-rheological measurements, scaling laws for the wall velocity gradient and the slip velocity with the wall shear stress were identified, and compared with results from the literature. Detailed microscopic measurements of the velocity field enabled an assessment of the effectiveness of a chemical treatment of the channel walls meant to suppress wall slip proposed by Metivier and coworkers, *Soft Matter* **8**, 2012.

An ubiquitous phenomenon observed during flows of yield stress materials along smooth solid surfaces is the slip of the velocity near the wall. From a phenomenological standpoint it is believed that the wall slip originates from the presence of a depleted layer of solvent near the solid surface and the bulk of the material "*slides*" over it. Some qualitative observations of the slip layer performed particularly for solid suspensions do exist [2, 3]. As Carbopol dispersions are concerned such observations are, to our best knowledge, practically absent in the literature.

As compared to the case of slip during flows of molecular (simple, or Newtonian) fluids where, based on the precise knowledge of the intermolecular forces, a rigorous theoretical framework may be derived [4, 5], the wall slip of yield stress materials remains elusive. A key step in understanding the physics of the wall slip in yield stress fluids is to reliably measure scaling laws of the slip velocity with respect to the wall shear stresses and the wall velocity gradients. The scaling behavior during flows of yield stress fluids in the presence of wall slip remains, however, an open topic. To substantiate this statement, we present in the following a brief literature review. The existing studies of wall slip during flows of yield stress fluids along smooth solid surfaces may be grouped in three distinct classes.

A first class refers to either phenomenological modelling and or numerical studies of the wall slip phenomenon, [6, 7]. Such studies typically rely on assumptions concerning the micro-structure of the material in vicinity of the solid wall which are often difficult to probe by means of direct visualisation. As the numerical studies are concerned, the evolution of the velocity gradients and stresses near the wall is typically obtained by assuming a known bulk rheological behaviour of material. Depending on the phenomenological assumptions being made, various slip laws are derived. The agreement between various phenomenological scaling predictions is, to our best understanding, not very satisfactory in the sense that various authors obtain different scaling results even when the same material is concerned which rarely match the experimental results, [6, 7].

A second and significantly broader class of studies refers to macroscopic experiments performed in either rheometric [8–14] or non-rheometric [15, 16] geometries. Such studies are sometimes combined with rather simple phenomenological models and scaling laws are obtained. The presence of wall slip complicates the determination of the yield stress [17] and systematically biases the assessment of the solid-fluid transition [15, 18].

A systematic experimental study of the wall slip phenomenon in a rheometric flow was reported by Meeker and coworkers, [8]. By assessing the slip behaviour via macro-rheological tests combined with measurements of the velocity geometry within the gap of the rheometric geometry, they identify three distinct slip regimes. They observed wall slip for applied stresses close to the yield stress τ_y whereas in a fully yielded regime this effect was negligible. A second macro-rheological study of the wall slip observed during flows of hard-sphere colloidal glasses was reported by Ballesta and coworkers, [10]. This study highlights only two slip regimes: solid (S) and fluid (F). Within the regime (S) a Bingham type slip regime is observed whereas within the (F) regime a Herschel-Bulkley slip behaviour is observed.

^{*} Eliane Younes Eliane.Younes@univ-nantes.fr

[†] Cathy Castelain Cathy.Castelain@univ-nantes.fr

[‡] Teodor Burghelca Teodor.Burghelca@univ-nantes.fr

[§] Volfango Bertola Volfango.Bertola@liverpool.ac.uk

The experimental study by Meeker and coworkers [8] is complemented by a phenomenological model based on micro-elasto-hydrodynamic lubrication picture which allows one to derive scaling laws for the full slip case. The main assumption behind this phenomenological approach is the existence of a depleted layer of solvent of width δ in the vicinity of the solid surface. However, the authors note that *"the slip layer is not resolvable in our setup, indicating that its thickness is smaller than $50\mu\text{m}$ "* meaning that during their experiments this assumption could not be probed by direct observation. A similar estimate of the layer thickness has been reported by Zhang and coworkers, [12]. Such small values explain why a direct visualisation of the depleted layer of solvent has never been reported in the literature.

A second sub-class of experimental macroscopic studies refers to non-rheometric flows such as laminar pipe flows. A study of the flow in the presence of wall slip in a glass-made capillary tube of a 0.2 wt% Carbopol gel was performed by Pérez-González et al. [16]. By combining the Particle Image Velocimetry technique with classical rheological measurements they found that the solid-fluid transition occurs gradually which complicates the determination of the yield stress. The authors estimate the wall velocity gradients using the relation between the imposed flow rate Q and the analytical solution of a fully developed Poiseuille flow for a Newtonian fluid. An experimental study of a laminar flow of a Carbopol gel in a glass made cylindrical pipe with a radius $R = 1.9\text{ mm}$ was performed by Poumaere and his coworkers [15]. Several important findings of this study can be summarised as follows. First, consistently with the findings of Pérez-González and coworkers, the transition from a solid like to a fluid like regime is smooth and mediated by an intermediate regime where the solid and fluid behaviors coexist. Second, the wall slip effects were found to be more pronounced around the yield point.

A third class of studies refers to microscopic flows where the influence of the confinement is expected to play an important role and can not be de-coupled from the wall slip and yielding behaviour, [19–22]. As compared to the second class, this third class of studies is somewhat less represented although the microscopic wall slip behaviour is relevant to a number of microscopic experimental settings such as the impact and/or atomisation of viscoplastic drops [23–26] with a number of applications in fuel industry and microscopic blood flows [27, 28].

Geraud et al. [20] studied the influence of confinement on the flow of a Carbopol microgel. They compare the bulk rheological behavior assessed via a macroscopic rheological tests and the velocity profiles measured in rough micro-channels. They found a strong disagreement between the bulk prediction of the velocity profiles and the ones measured in the micro-channels and they attribute this discrepancy to the confinement of the flow. Liu et al. [19] compared the measured velocity profiles in micro-channels to simulations performed based on the bulk rheology. They show that the confinement effects become important when the dimensions of the channel are comparable to the characteristic size of the material's microstructure and, consequently, the measured velocity profiles differ from those computed numerically using the Herschel-Bulkley constitutive relation. These studies address the effects of the confinement on the flow behaviour and provide some information on the wall slip phenomenon as well.

Most recently, Péméja and coworkers have presented a systematic experimental investigation of wall slip regimes of a Carbopol gel in a micro-channel, [22]. As in Ref. [16] the authors compute the wall shear stress using the pressure drop. To rationalise their results, the authors use a phenomenological model similar to the one proposed by Meeker and coworkers in Ref. [8]. Based on measurements of the transversal profiles of the axial velocity, they identify two distinct scaling regimes as the driving pressure drops are gradually increased. Seth and coworkers studied the slip behaviour in a microscopic rotational shear cell (Linkam CSS 450) by means of Particle Tracking Velocimetry, [29]. They identify two slip regimes separated by an abrupt transition. For stresses exceeding the yield stress $\tau > \tau_y$, the slip velocity scales linearly with the stress and the slope of this linear dependence does not depend on the chemistry of the solid surface. In the plug flow regime ($\tau < \tau_y$), the slip velocity measured at an imposed stress is very sensitive to the nature of the surfaces. To rationalise their findings, the authors use an elasto-hydrodynamic lubrication model which allows them to compute the wall shear stress as a function of the slip velocity and the thickness δ of the lubricating layer. A microscopic study of the slip behaviour of a soft glassy material is presented by Mansard and coworkers, [30]. They highlighted a strong dependence of the slip behaviour on the degree of roughness of the solid surface which was accurately controlled by means of micro-patterning using standard micro-photolithography procedure.

An important conclusion that can be drawn from the existing experimental studies performed in macroscopic or microscopic geometries is that the wall slip behaviour can not be de-coupled from the yielding behaviour. Unlike in the case of the polymer melts where the wall slip emerges at large rates of strain [31, 32], in the yield stress materials the picture is strikingly different. All the experiments reviewed above indicate that the wall slip effects are more pronounced in a range of low shear rates (where the solid-fluid transition takes place) and are significantly less important far beyond the yield point when a simple constitutive equation (such as the Herschel-Bulkley constitutive law) is reliable, [15, 18]. Whereas about this fact there seems to be a general consensus within the viscoplastic community, various authors use different assumptions (which in most of the cases could not be verified by means of direct visualisation of the flow in windows sufficiently small and close to the solid boundary) and phenomenological models (e.g. the elasto-hydrodynamic lubrication model sometimes combined with yet other assumptions on the nature of intermolecular forces responsible for the wall slip) in order to rationalise their findings and obtain scaling laws. An additional drawback of some of the previous studies relates to using questionable correlations (e.g. computing the wall shear rate using the flow rate or pre-assuming a Herschel-Bulkley like velocity profile which, as shown in Ref. [19]) is not accurate in the presence of confinement. The overall conclusion is that, in spite of the reliability of the macroscopic scale experiments in capturing the wall slip behaviour, there seems to exist no universal consensus on neither the scaling behaviour

nor the fundamental physical mechanisms responsible for the wall slip behaviour.

The central aim of the present contribution is to provide a systematic experimental characterization of the microscopic wall slip phenomenon in terms of scaling laws of the slip velocity with both the wall shear stresses and the wall velocity gradients. The novelty of the approach we propose in the following consists of assessing these scaling laws by judiciously correlating microscopic measurements of the wall velocity gradients performed in a plane micro-channel with the bulk rheological behaviour assessed by macro-rheological measurements performed in a steady state. By doing so we avoid making any of the assumptions other authors made such as the presence of a lubricating layer and/or a constitutive relation and/or the relationship between the wall shear stresses and the driving pressures. The study is complemented by a investigation of the effectiveness of a chemical treatment of the channel walls meant to suppress the wall slip.

The paper is organised as follows. The rheological characterization of the working fluid is presented in Sec. I A. The design of micro-channel setup as well as the data acquisition protocol are presented in Sec. I B. The data analysis procedure is discussed in Sec. I C. A systematic characterization of the velocity profiles is presented in Sec. II. By combining the micro-fluidic and macro-rheological measurements, we identify in Sec. II B different scaling laws of the wall slip phenomenon corresponding to different flow regimes. A detailed comparison of the experimentally found scaling laws with the results from the literature is presented in Sec. II C. In Sec. III we explore the possibility of inhibiting the wall slip via a chemical treatment of the micro-channels. The paper closes with a summary of the main conclusions and a discussion of several perspectives this study may open, Sec. IV.

I. Experimental methods

A. Choice, preparation and rheological characterization of the working fluid

We chose a Carbopol gel as a working fluid. The rationale behind this choice is the following. First, such gels are optically transparent which allows an in-situ visualisation of their flows and subsequent measurements of the flow fields. Second, they are chemically stable over extended periods of time. Third, and foremost, the Carbopol gels have been considered as “*model*” yield stress materials for over two decades [33–35]: they practically exhibit no thixotropy and their deformation may be described by the Herschel-Bulkley law.

However, it has been shown recently that even in the case of a Carbopol gel, the solid-fluid transition does not occur at a well defined value of the applied stress but gradually (within a finite range of stresses and, when forced in an unsteady fashion, they equally exhibit weak thixotropic effects manifested through a rheological hysteresis which is related to the degree of steadiness of the forcing, [26, 36–40]). In addition to that, the Herschel-Bulkley constitutive relationship can not reliably describe the deformation states within the transitional regime.

To avoid such time-dependent effects which may bias the slip behaviour, we focus through this paper on steady state microscopic flows which we correlate to steady state rheological measurements.

1. Fluid preparation

The working fluid was an aqueous solution of Carbopol Ultrez 10 with the concentration of 0.1 wt%. Carbopol is the generic trade name of a cross-linked polyacrylic acid $-[CH_2 - CH(COOH)]-$ with high molecular weight. In an anhydrous state, it is commercialized in the form of a white powder soluble in aqueous solvents. After the addition of a neutralising agent such as sodium hydroxide (*NaOH*), a clear gel is obtained. The Carbopol gels exhibit an elasto- viscoplastic rheological behaviour in a neutral state due to the presence of a jammed spongy microstructure, [37, 41, 42].

The Carbopol gel was prepared according to the following protocol. First, the right amount of anhydrous Carbopol was dissolved in deionized water using a magnetic stirring device at a speed of 1000 rpm. The degree of mixing/dissolution was assessed visually by monitoring the optical isotropy of the solution. Next, the *pH* of the solution was gradually increased from 3.2 to 7 by gradual titration with a small amount of a 10 wt% aqueous *NaOH* solution gradually pipetted while gently mixing the solution. The rheological tests were performed after seeding the Carbopol solution with the fluorescent tracers as detailed in Sec. I B. The average density of the Carbopol solution was $\rho \approx 1100 \text{ kg.m}^{-3}$.

2. Rheological measurements

The rheological measurements were performed using a controlled stress rotational rheometer (Mars III, Thermofischer Scientific) equipped with a nano-torque module. Tests were performed using a parallel plate geometry with a diameter $D = 35 \text{ mm}$ and a gap $d = 1 \text{ mm}$. To prevent the wall slip, glass paper with an average roughness of $500 \mu\text{m}$ was glued on each plate. To account for the addition of the glass paper on the rotating plate of the device, the inertia of the device was recalibrated. The absence of any wall slip effect was verified by measuring flow curves in subsequent tests performed with several values of the gap and showing that all measurements perfectly overlap. To prevent the evaporation of the solvent during the rheological measurements a thin layer of commercial oil was added to the free meniscus of the sample.

Rheological measurements were performed according to the following protocol. First, the sample was pre-sheared at a constant applied stress larger than the yield stress for 300 s and allowed to relax for another 300 s. Then, to assess the rheological behavior of the Carbopol gel in different deformation regimes, a commonly used rheological test consisting of loading the material according to an increasing stress ramp was applied to a fluid sample. The duration of each step was $t_0 = 5 \text{ s}$ and the data averaging time per stress value was $\delta t_0 = 2 \text{ s}$.

165 To test the reproducibility and quantitatively assess the instrumental error, each rheological measurement was repeated three
 166 times with a fresh sample. A rheological flow curve obtained by averaging the results of three distinct measurements is illustrated
 167 in Fig. 1. The error bars are defined by the standard deviation of the three data sets.

168 Three distinct deformation regimes consistent with previous macro rheological investigations, [26, 37–40, 43] are observed.
 169 For low values of applied stress, the variation of the rate of material deformation $\dot{\gamma}$ with the applied stress is negligibly small.
 170 This corresponds to a solid-like behavior of the material, region **(S)** in Fig. 1. For high values of applied stress (beyond the yield
 171 stress), the material becomes fully yielded, region **(F)** in Fig. 1, and its behavior follows the Herschel-Bulkley fit, the red line in
 172 Fig. 1.

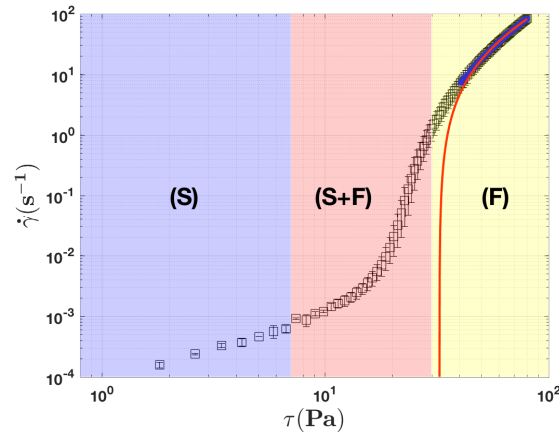


Figure 1. Dependence of the shear rate $\dot{\gamma}$ on the on the applied stress τ . The red line represents the Herschel - Bulkley fit that gives $\tau_y = 32.5 \pm 2.5 Pa$, $K = 2.8 \pm 0.215 Pa \cdot s^n$, $n = 0.6403 \pm 0.0299$. The symbols marking the highlighted regions denote the deformation regimes and are explained in the text: **(S)** - solid, **(S + F)** - solid-fluid coexistence, **(F)** - fluid.

173 For intermediate values of the applied stresses, the solid- fluid transition is not direct and the behavior of the material corre-
 174 sponds neither to a solid-like regime nor to a viscous flow regime, region **(S+F)** in Fig. 1. Based on the Herschel-Bulkley fit, the
 175 yield stress of the working material is around $\tau_y \approx 32.5 Pa$.

176 A natural question one may ask at this point is to what extent the steady state rheological measurements presented in Fig. 1
 177 are relevant to the steady micro-channel flow under investigation. As shown in Refs. [26, 37] for characteristic times per stress
 178 step t_0 larger than $2s$ (we recall that the rheological data was acquired with $t_0 = 5s$) the regimes **(F)** and **(S+F)** are practically
 179 independent of t_0 while a weak dependence is always observed in the regime **(S)**. This means that as long as we restrict ourselves
 180 to the regimes **(F)** and **(S+F)**, a meaningful correlation between the rheological measurements presented in Fig. 1 and the flow
 181 fields measured in the micro-channel can be made. For a more systematic analysis of the influence of rate at which Carbopol
 182 gels are loaded during controlled stress ramps on the rheological response the reader is referred to Refs. [26, 44].

183 B. Micro-channel design, microscopic flow control and data acquisition protocol

184 The experiments have been performed in a straight micro-channel. The width of the micro-channel is $W = 200 \mu m$, its depth
 185 is $H = 200 \mu m$ and its length $L = 4 cm$. A micrograph of the channel is presented in Fig. 2.

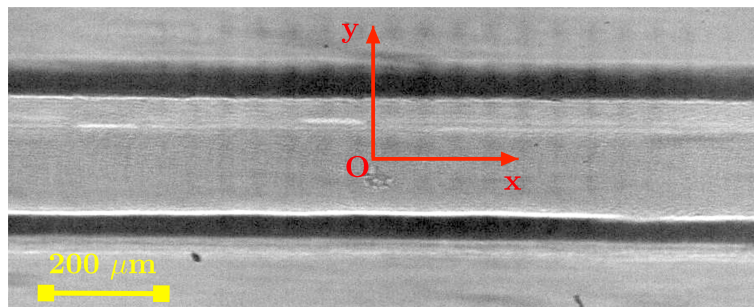


Figure 2. Micro-graph of the micro-channel. The image was acquired in white light.

186
 187 The micro-channel was machined in an acrylic block with the dimensions $5 cm \times 3 cm \times 0.5 cm$ using a fast spinning
 188 (14000 *rot/min*) micro-milling head (Nakanishi, model *HES510 - BT40*) mounted on a commercial computer controlled milling
 189

190 machine (Twinhorn, model *VH1010*). By a precise alignment of the initial acrylic block on the stage of the milling machine,
 191 the depths of the micro-channel were uniform over its entire lengths with an end to end variation smaller than one percent. The
 192 average roughness of the edges of the micro-channel as resulted from the micro milling process is roughly of the order of a mi-
 193 cron which accounts for half percent of the channel width. This point is fully supported by the micrograph of the micro-channel
 194 shown in Fig. 2. We note that this level of edge smoothness is comparable to that obtained via the classical micro lithography
 195 techniques used to produce PDMS micro-channels, [45]. The micro-channel was sealed with a strong and optically transparent
 196 adhesive tape (3M, model 727 – 1280). The micro-channel chip is mounted on an inverted epifluorescent microscope (Axio
 197 Observer A1, serial no3832002215.), Fig. 3.

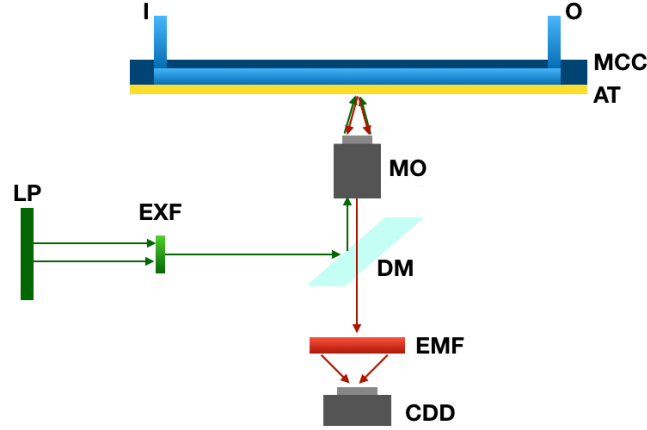


Figure 3. Schematic view of the microfluidic experimental setup: MCC: micro-channel chip, I: micro-channel inlet, O: micro-channel outlet, AT: adhesive tape, MO: microscope objective, DM: dichroic mirror, LP: light emitting lamp, EXF: excitation filter, EMF: emission filter, CCD: digital camera.

198 The microscopic flows have been visualised through a 20X magnification objective (Zeiss EC Plan-NEOFLUAR 20x/0,5)
 199 with a numerical aperture $NA = 0.35$ and a long working distance $WD = 70 \text{ mm}$. The microscopic flows were generated using a
 200 high precision micro-syringe pump (KdScientific, model Legato 110). To insure a steady flow rate Q which was crucial for this
 201 study, we have used a 10 ml gas tight syringe (Hamilton, model 1010LT). The flows were illuminated with a powerful halogen
 202 lamp coupled to the inverted microscope. To visualise the flow, the working fluid was seeded with a minute amount of buoyantly
 203 neutral fluorescent tracers with a diameter of $0.92 \mu\text{m}$ (Fluoresbrite Multifluorescent from Polysciences). A series of 1000 flow
 204 images was acquired corresponding to each value of the flow rate Q with a digital camera. The images were acquired at the mid-
 205 plane of the micro-channel and at mid-distance downstream. For the experiments where the flow rate did not exceed $10 \mu\text{L}/\text{min}$,
 206 we have used a Prosilica GE camera with 16 bit quantisation (model GE680C from Allied Technologies). The maximal frame
 207 rate achievable with this camera is 200 fps . During the experiments with flow rates $Q \in [10, 23] \mu\text{L}/\text{min}$, a Mikrotron camera
 208 has been used up to a frame rate of 500 fps .

209 C. Data analysis

210 The main tool used to systematically characterize the microscopic flow was an adaptive multi-grid Digital Particle Image
 211 Velocimetry (DPIV) (see Refs. [46, 47] for a detailed description of the method) entirely developed in house under Matlab
 212 (together with the “Image Processing Toolbox”) which followed the steps briefly described below. The first step of the data
 213 acquisition procedure was to precisely identify the borders of the micro-channel. Though apparently trivial, this step is crucial
 214 for correctly measuring the slip velocity and the wall velocity gradients which represent the core of the present study. To do
 215 so, we have build from the entire sequence of acquired images a space time diagram $xt = xt(t, y)$ of the transversal (to the flow
 216 direction) profiles of image brightness acquired at the middle of the field of view., Fig. 4(a). Next, we have computed the root
 217 mean square deviation (rmsd) of the space-time diagram along its temporal axis according to:

$$I^{rms}(y) = \left(\langle (xt(t, y) - \langle xt(t, y) \rangle_t)^2 \rangle_t \right)^{1/2} \quad (1)$$

218 Here $\langle \cdot \rangle_t$ denotes the average of a two dimensional array computed along its temporal dimension t . Last, we identify the edges
 219 of the channel by the finding the two local maxima of the dependence $\left| \frac{dI^{rms}(y)}{dy} \right|$ represented in Fig. 4(b) by the circles.

220 Second, a background was calculated by averaging all the images of the first time series we have acquired. Third, the average
 221 background was subtracted from images. Finally, pairs of pre-processed images separated in time by the inter-frame t_1 are
 222 passed to a multi-pass DPIV algorithm using a sequence of squared interrogation windows with sizes $[128, 64, 32, 16, 8]$. As a

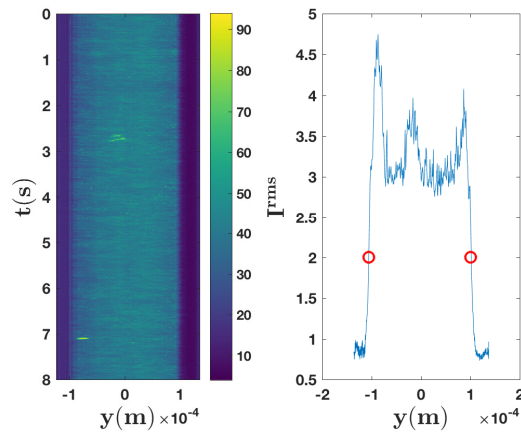


Figure 4. The plot on the left refers to the space time of the transversal profiles of image brightness acquired at the middle of the field of view. The plot on the right refers to the root mean square deviation (rms) of the brightness of the space time diagram along the temporal direction.

223 post-processing step, each computed velocity field obtained from the *DPIV* algorithm was filtered using a median filter. The
 224 spatial resolution of the velocity fields was $4.5 \mu m$ (44 times smaller than the width of the channel) which suffices for a reliable
 225 calculation of the velocity gradients in the proximity of the channel walls. Corresponding to each driving flow rate, we have
 226 computed the average of 1000 subsequent velocity fields together with their root mean square deviation (rms) which allowed
 227 one to specify error bars.

228 To compute accurately the velocity gradients, each profile of the time averaged velocity was first fitted by a smoothing
 229 spline function which was differentiated analytically in order to avoid the inherent errors associated to the classical numerical
 230 differentiation.

231 To extract the wall slip velocity, we have extrapolated each spline fitting function of the axial velocity and computed its value
 232 at the level of the wall. The velocity gradient near the wall was assessed via the slope of the last four points of the smoothing
 233 spline function. The size of the rigid plug located along the centre-line of the micro-channel was estimated by detecting the
 234 position where the transversal gradient of the axial velocity becomes larger than 0.3 % of its maximal value along the velocity
 235 profile. The plug velocity was calculated by averaging the velocity within the plug region.

236 II. Results

237 A. Description of the flow regimes in the presence of wall slip

238 We focus in the following on the experimental characterization of the microscopic flow profiles of a Carbopol gel in a steady
 239 channel flow for several flow rates.

240 Profiles of the time averaged flow velocity U_{av} measured according to the method described in Sec. IC are presented in Fig. 5.
 241 Due to the axial symmetry of the flow, velocity profiles were plotted only across half width of the channel ($y = 0$ corresponds to
 242 the centreline of the micro-channel and $y = 1 \times 10^{-4} m$ corresponds to the channel wall.). The standard deviation of the velocity
 243 profiles was smaller than 5% for different values of flow rates. Depending on the magnitude of the constant imposed flow rate
 244 Q , three distinct flow regimes are observed in Fig. 5.

245 At low driving flow rates ($Q < 2 \mu l/min$), a full plug flow regime is observed in Fig. 5(a). The entire Carbopol gel is
 246 unyielded and, according to some authors (e.g. see Refs. [35, 48]), it “slides” over a very thin liquid layer located in the proximity
 247 of the channel walls. We once more emphasise, however, that this simple phenomenological picture has not been yet confirmed
 248 by direct visualisation of the solid material units during the flow. The full plug velocity profiles are characteristic of a solid-like
 249 behavior visible in Fig. 1 (region **(S)**) and phenomenologically consistent with the observations of Pérez-González et al. [16].

250 As the flow rate is gradually increased past this first flow regime, a second flow regime is observed. The Carbopol gel is
 251 partially yielded in the proximity of the channel walls (where the velocity gradients are the largest) but a central un-yielded plug
 252 may still be observed around the centre-line of the micro-channel, Fig. 5(b). The shear stresses are not large enough to yield the
 253 material along the entire width of the channel. This behaviour might be related to the solid-fluid transition **(S+F)** of the material
 254 observed in Fig. 1 where the solid and fluid material elements coexist.

255 As the flow rate is increased even further ($Q > 10 \mu l/min$), the Carbopol gel is fully yielded across the entire width of
 256 the channel in the sense that the central plug becomes negligibly narrow which is qualitative indicator that this flow regime
 257 corresponds to the fluid rheological regime **(F)** observed in Fig. 1.

258 As a more quantitative argument, we note that the velocity profiles presented in Fig. 5(c) may be well fitted by the analytical

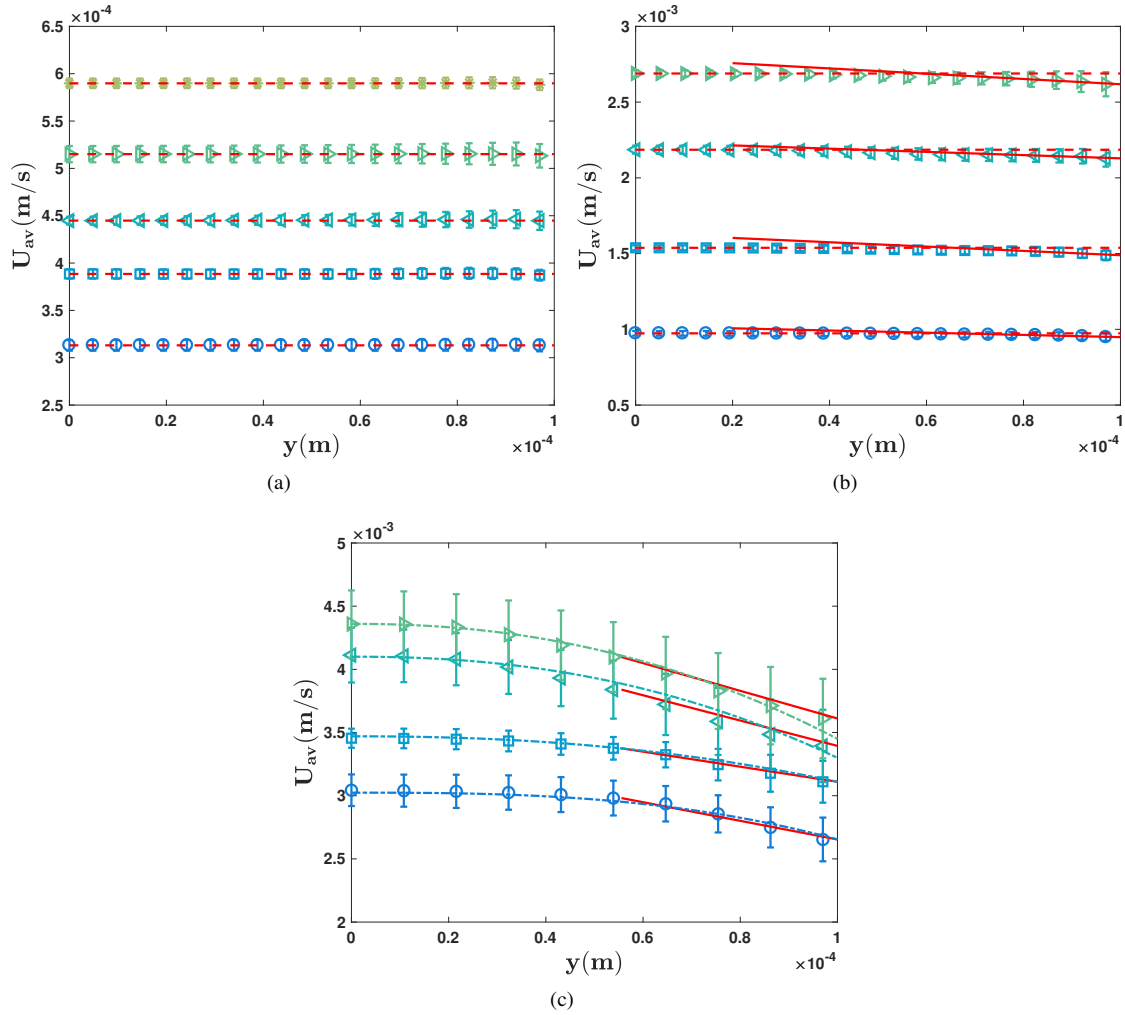


Figure 5. Velocity profiles for different values of flow rate Q . Panel (a) corresponds to the solid regime: circles- $Q = 1 \mu\text{l}/\text{min}$, squares- $Q = 1.4 \mu\text{l}/\text{min}$, left triangles- $Q = 1.6 \mu\text{l}/\text{min}$, right triangles $Q = 1.8 \mu\text{l}/\text{min}$, stars- $Q = 2 \mu\text{l}/\text{min}$. Panel (b) corresponds to the transition: circles- $Q = 3.5 \mu\text{l}/\text{min}$, squares- $Q = 5.5 \mu\text{l}/\text{min}$, left triangles- $Q = 8 \mu\text{l}/\text{min}$, right triangles $Q = 10 \mu\text{l}/\text{min}$. Panel (c) corresponds to the fluid regime: circles- $Q = 14 \mu\text{l}/\text{min}$, squares- $Q = 15 \mu\text{l}/\text{min}$, left triangles- $Q = 21 \mu\text{l}/\text{min}$, right triangles $Q = 23 \mu\text{l}/\text{min}$. The dash dotted lines are fitting functions according to analytical solution of the Poiseuille flow of a power law fluid given by Eq. 2. To better visualise the plug region, dashed horizontal lines are plotted in panels (a,b).

259 solution of the Poiseuille flow of power law fluid, [49]:

$$U_{av} = U_s + C \left[1 - \left(\frac{2y}{W} \right)^{1+\frac{1}{n}} \right] \quad (2)$$

260 where the pre-factor C is a fit parameter and $n \approx 0.64$ is the power law index of the Carbopol gel obtained via a Herschel-Bulkley
261 fit (see Fig. 1).

262 Corresponding to each flow regime, the velocity profiles clearly exhibit a slip behavior at the channel walls (a non-zero slip
263 velocity at $y = 1 \times 10^{-4} \text{ m}$). The measured slip velocity is systematically larger than the error bar of the velocity profile near the
264 wall.

265 The measured velocity profiles allow one to compute the velocity gradients near the wall, the slip and plug velocities and the
266 plug size W_p defined by the extent of the flat central region. The evolution of the size of the rigid plug W_p with the flow rate
267 is presented in Fig. 6. At low values of flow rate ($Q < 2 \mu\text{l}/\text{min}$) the plug size is practically independent on the flow rate: the
268 plug fills the entire width of the channel. Beyond ($Q \approx 2 \mu\text{l}/\text{min}$) the plug size decreases as Q is increased. The shear stresses
269 are not large enough to yield the material along the entire width of the micro-channel. Beyond a critical value of the flow rate
270 ($Q > 10 \mu\text{l}/\text{min}$), a plug is no longer observed ($W_p \approx 0$) and the material becomes fully yielded. In this case the local shear

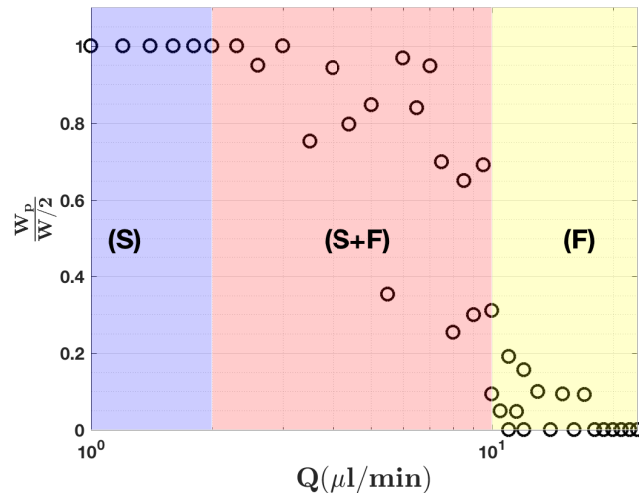


Figure 6. Dependence of the normalized plug width $2W_p/W$ on the applied flow rate Q . The symbols marking the highlighted regions denote the deformation regimes and are explained in the text: **(S)** - solid, **(S + F)** - solid-fluid coexistence, **(F)** - fluid.

271 stresses exceed the yield stress nearly everywhere across the channel width except (perhaps) for a narrow region centred around
 272 the local maximum of the velocity profile which can not be resolved by our measurements.

273 B. Scaling behavior at the wall within various flow regimes

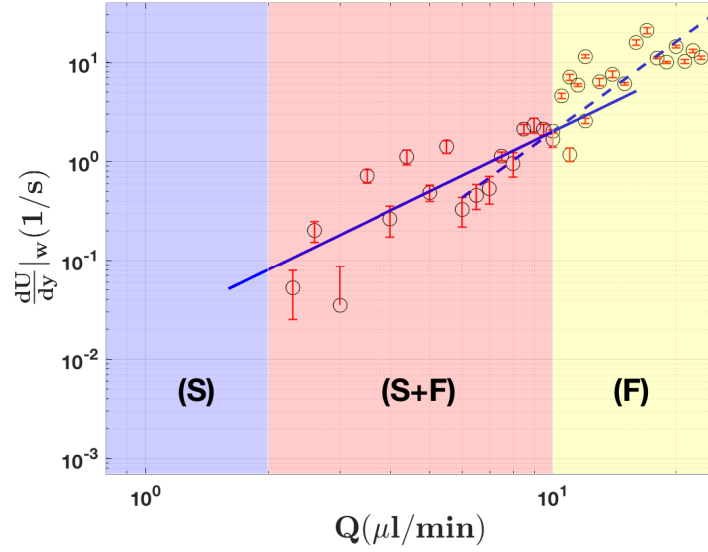
274 As already emphasised in the introduction, understanding the scaling behavior of the relevant hydrodynamic quantities (shear
 275 stress, shear rate, slip velocity) in the proximity of the wall is of paramount importance to developing reliable microscopic
 276 models able to explain the confined flows of viscoplastic materials in the presence of wall slip and for the implementation of
 277 numerical simulations. Based on the characterization of the flow fields presented in Sec. II A, we study in this section the scaling
 278 behavior for each flow regime previously identified.

279 The dependence of the wall velocity gradients computed according to the procedure detailed in Sec. I C on the flow rate Q
 280 is presented in Fig. 7(a). As the fair amount of scatter of the data prevented us from reliably performing a power law fit, the full
 281 and dashed lines are only guides for the eye. In the solid region **(S)**, the material is fully unyielded and, within the instrumental
 282 accuracy of our technique, no velocity gradients could be reliably measured near the solid wall. As the flow rate Q is gradually
 283 increased, one can clearly notice the existence of two different scaling regimes. Within the solid-fluid transition regime **(S+F)**,
 284 the wall velocity gradient scales with the flow rate as $\frac{dU}{dy}|_w \propto Q^2$ (see full line in Fig. 7(a)). A further increase of the flow rate
 285 into the fluid regime **(F)** leads to a different scaling of the wall velocity gradient, $\frac{dU}{dy}|_w \propto Q^3$ (see dashed line in Fig. 7(a)).

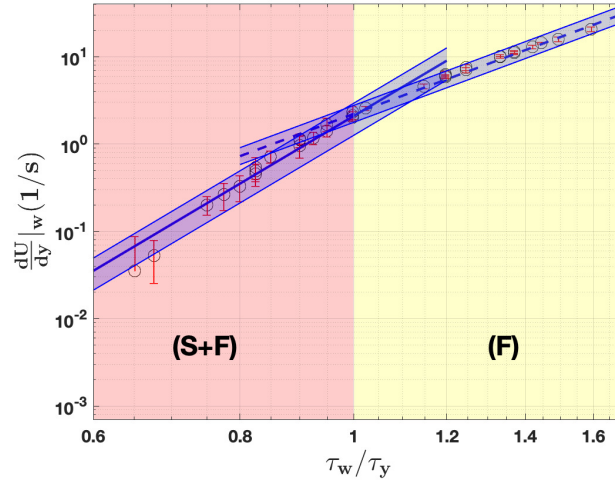
286 The measurements of the wall velocity gradients $\frac{dU}{dy}|_w$ allow one to compute the wall shear stresses τ_w using the macro-
 287 rheological measurements presented in Fig. 1. To do so, we interpreted $\frac{dU}{dy}|_w$ as the relevant scale for the rate of shear and
 288 interpolated the corresponding stress from the macro-rheological flow curve presented in Fig. 1. The result of this evaluation is
 289 presented in Fig. 7(b). Two different scaling regimes of the wall shear rate with the wall shear stress can be clearly observed.
 290 The first scaling regime corresponds to a partial yielding of the gel in the vicinity of the wall, $\frac{dU}{dy}|_w \propto \tau_w^{8 \pm 0.5}$ (see solid line in
 291 Fig. 7(b)). Above a critical value of wall shear stress and corresponding to the fluid deformation regime a second scaling regime
 292 is observed, $\frac{dU}{dy}|_w \propto \tau_w^{5 \pm 0.3}$ (see dashed line in Fig. 7(b)). The blue shaded regions overlapped onto the power laws indicate the
 293 error bounds of the power law fitting functions.

294 The data presented in Fig. 7(b) prompt us to revisit the dependence of the plug size W_p presented in Fig. 6. According to
 295 Fig. 7(b) the maximum value of the wall shear stress is, $\tau_w^{max} \approx 1.8\tau_y$. If the microscopic flow was accurately described by
 296 the Herschel-Bulkley analytical solution (for the analytical solution we refer the reader to Ref. [50]) then the minimum size of
 297 the solid plug W_p corresponding to the maximum wall shear stress τ_w^{max} should be $W_p = \frac{\tau_y}{\tau_w^{max}} W \approx 0.55W$. As the instrumental
 298 resolution of the plug measurements presented in Fig. 6 would certainly allow detecting such value, we can only conclude at
 299 this point that the theoretical prediction for the plug width based on the Herschel-Bulkley law does not work in this case. This
 300 conclusion corroborates well with the lack of applicability of the Herschel-Bulkley model in describing confined microscopic
 301 flows of a Carbopol gel discussed in Refs. [19, 20].

302 The scaling exponent obtained by fitting the data corresponding to the fully yielded regime differs from the power law exponent
 303 obtained by the Herschel-Bulkley fitting to the macro-rheological measurements. This difference might be attributed as well
 304 to the confinement, [19, 20]. However, we can notice that the value of the critical wall shear stress defined as the intersection



(a)



(b)

Figure 7. (a) Dependence of the wall velocity gradient on the applied flow rate Q . The solid line (-) and the dashed line (- -) are guides for the eye, $\frac{dU}{dy}|_w \propto Q^2$ and $\frac{dU}{dy}|_w \propto Q^3$ respectively. (b) Dependence of the wall velocity gradient on the reduced wall shear stress τ_w/τ_y , computed using the rheological measurements and computed wall velocity gradients. The solid line (-) and the dashed line (- -) are power law fitting functions, $\frac{dU}{dy}|_w \propto \tau_w^{8 \pm 0.5}$ and $\frac{dU}{dy}|_w \propto \tau_w^{5 \pm 0.3}$ respectively. The blue shaded regions overlapped onto the fit functions represent the error bounds of the power law fitting functions.

305 between the two power laws is close to the yield stress measured in the rheometric flow and fitted by the Herschel-Bulkley
 306 model, see Fig. 1.

307 The dependence of the slip velocity U_s on the wall shear stress τ_w is presented in Fig. 8(a). Because in the solid regime the wall
 308 velocity gradients are too small to be reliably measured, we could not use the method described above to reliably compute the
 309 wall shear stresses. For higher flow rates (beyond the (S) regime), again, two distinct scaling laws are observed. Corresponding
 310 to the solid-fluid coexistence regime (S+F), $U_s \propto \tau_w^{3.5}$. Within the fully yielded regime (F), $U_s \propto \tau_w$.

311 The dependence of the slip velocity U_s on the wall velocity gradients $\frac{dU}{dy}|_w$ is illustrated in Fig. 8(b). Within the (S + F) and
 312 (F) $\frac{dU}{dy}|_w$ scales as $U_s \propto \left(\frac{dU}{dy}|_w\right)^{0.5}$ and $U_s \propto \left(\frac{dU}{dy}|_w\right)^{0.2}$, respectively.

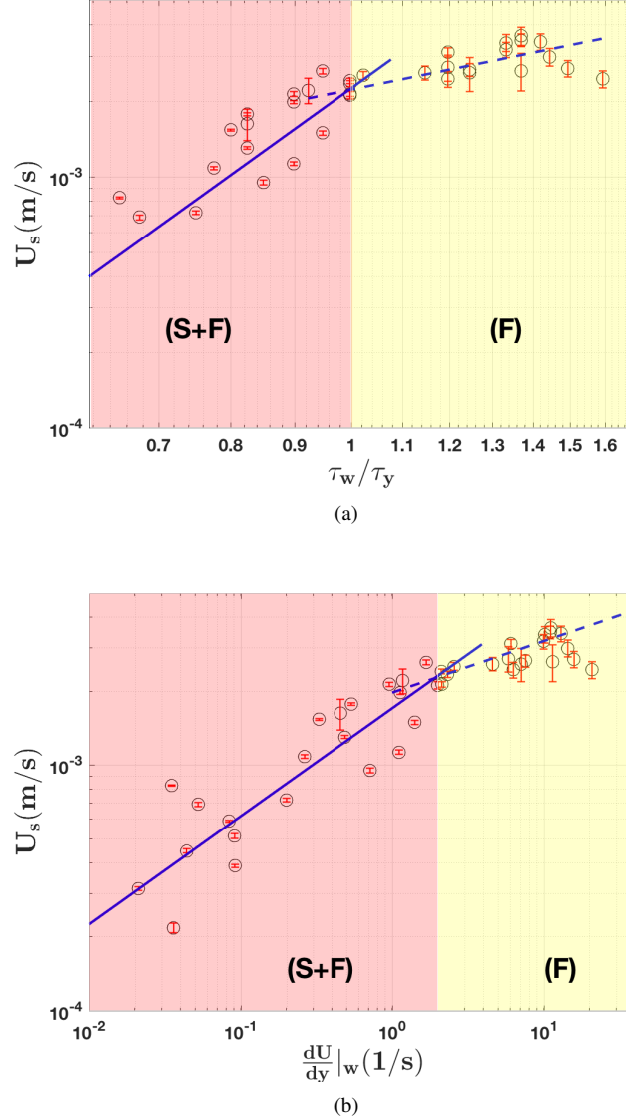


Figure 8. (a) Dependence of the wall slip velocity U_s on the wall shear stress τ_w . The full (—) and dashed (---) lines are guides for the eye, $U_s \propto \tau_w^{3.5}$, $U_s \propto \tau_w$ respectively. (b) Dependence of the wall slip velocity U_s on the wall velocity gradient $\frac{dU}{dy}|_w$. The full (—) and dashed (---) lines are guides for the eye, $U_s \propto \left(\frac{dU}{dy}|_w\right)^{0.5}$ and $U_s \propto \left(\frac{dU}{dy}|_w\right)^{0.1}$ respectively. The symbols marking the highlighted regions denote the deformation regimes and are explained in the text: **(S + F)** - solid-fluid coexistence, **(F)** - fluid.

313

C. Comparison with previous results from the literature

314 We compare in the following the scaling laws described in Sec. II with results obtained by others.

315 Pérez-González et al. have investigated the scaling behaviour in a millimetre size glass channel, [16]. They have estimated
 316 the apparent shear rate $\dot{\gamma}_a$ and the wall shear stress τ_w as $\dot{\gamma}_a = \frac{32Q}{\pi D^3}$, $\tau_w = \frac{\Delta P}{4L}$ respectively, where ΔP is the pressure drop between
 317 the capillary ends, L and D are respectively the length and the diameter of the borosilicate glass capillary and Q is the flow rate
 318 calculated from the integration of the velocity profiles. Consistently with our findings, they identify three distinct flow regimes:
 319 a purely plug flow before yielding, solid- liquid transition and shear thinning at relatively high shear rates. The apparent shear
 320 rate $\dot{\gamma}_a$ scales with the wall shear stress τ_w as $\dot{\gamma}_a \propto \tau_w^{2.5}$ in the fluid regime. This scaling law differs significantly from the one we
 321 observe, $\frac{dU}{dy}|_w \propto \tau_w^5$ (the dashed line in Fig. 7(b)). This difference might be related to the way $\dot{\gamma}_a$ is calculated ($\dot{\gamma}_a = \frac{32Q}{\pi D^3}$). This
 322 formula assumes that the velocity profile is parabolic and there exists no velocity slip at the walls which, obviously, is not the
 323 case for a Carbopol gel flowing in a glass capillary.

324 By direct observation of a rheometric flow of a microgel, Meeker et al. in Ref. [51] observe that U_s remains constant for

325 $1 < \frac{\tau}{\tau_w} < 1.5$ while in our experiments the slip velocity increases linearly with the wall shear stress, $U_s \propto \tau_w$.

326 The same authors observe in a subsequent publication three slip regimes in a macro-rheological setup, [8]. In a solid regime
327 they find a slip velocity that scales as the stress squared whereas in the intermediate deformation regime they find a constant slip
328 velocity. These scaling results are obtained within the framework of a phenomenological microelastohydrodynamic lubrication.
329 As we use no model for assessing the scaling behaviour, a comparison is rather difficult to make.

330 Péméja and coworkers have obtained two wall slip scaling laws for the micro-channel flow of a Carbopol gel: for low wall
331 shear stresses $\tau_w < 100 \text{ Pa}$ $U_s \propto \tau_w^2$ whereas for higher stresses they obtain a linear scaling. The quadratic scaling law is at
332 odds with the result presented in Fig. 8(a), $U_s \propto \tau_w^{3.5}$ whereas the linear scaling law is consistent with our findings. This partial
333 agreement may be explained by the way Péméja compute the wall shear stress using the driving pressure drop Δp , $\tau_w = \frac{h}{2L} \Delta p$
334 (L being the length of their micro-channel and h its depth). This correlation may become relatively accurate "only" far from the
335 yield point whereas it is most probably formal in the solid (S) and in the intermediate (S+F) regimes.

336 To describe the wall slip behavior Kaylon proposed the following relationship between the slip velocity and the wall shear
337 stress [17]:

$$U_s = \beta(\tau_w)^{1/n_b} \quad (3)$$

338 Here β relates the width of the slip layer δ to the consistency of the binder fluid m_b and to its power-law index n_b , $\beta = \frac{\delta}{m_b^{1/n_b}}$. This
339 simple phenomenological scaling relationship is derived based on the assumption of the existence of a depleted layer of solvent
340 of width δ in the proximity of the solid boundary (such assumption is often used in order to derive simple phenomenological
341 scaling models, e.g. see Ref. [12]). The Carbopol gel is considered as jammed system of swollen gel micro-particles [35]. As
342 the solvent of the Carbopol gel was deionised water, the "binder fluid" might be considered as Newtonian, $K_b = 10^{-3} \text{ Pa}\cdot\text{s}$ and
343 $n_b = 1$.

344 In the fluid regime, U_s scales linearly with τ_w , $U_s \propto \tau_w$ (the dashed line in Fig. 8(a)). The full/dashed lines are guides for the
345 eye. This linear scaling law confirms the assumption that the "binder fluid" is Newtonian, $n_b = 1$. A similar scaling law was
346 found by Poumaere et al. [15] while it differs from the ones predicted theoretically by Piau [35] $U_s \propto \tau_w^{1/3}$ for loosely packed
347 system and $U_s \propto \tau_w^2$ for closely packed system. This difference might be related to the fact that the lubricating fluid is considered
348 as non-Newtonian fluid in Ref. [35].

349 In our study, the measured factor $\beta = 70 \cdot 10^{-6} \text{ m}\cdot\text{Pa}^{-1}\cdot\text{s}^{-1}$ leads to a slip layer of thickness $\delta \approx 0.07 \mu\text{m}$. This value is of the
350 same order of magnitude as the one found by Jiang et al. [52], $\delta \approx 0.1 \mu\text{m}$ and by Poumaere et al. [15], $\delta \approx 0.23 \mu\text{m}$. However,
351 this width obtained by such simple estimates is far too small to be accessible via direct visualisation of the flow meaning that, the
352 main hypothesis used to predict this scaling remains for now just a hypothesis. This once more justifies our approach of relying
353 on no assumption but computing the stresses by relating the steady state rheological behaviour to the in-situ measurements of
354 the wall velocity gradients.

355 The dependence of the slip velocity on the wall velocity gradient is presented in Fig. 8(b). Once more, due to the rather
356 large scatter of the data, the full/dashed lines are just guides for the eye. Within the S+F regime we observe a dependence
357 $U_s \propto \left(\frac{dU}{dy}\bigg|_w\right)^{0.5}$ whereas in the fluid regime (F) the scaling behaviour changes to $U_s \propto \left(\frac{dU}{dy}\bigg|_w\right)^{0.2}$.

358 III. On the possibility of inhibiting the wall slip in an acrylic made micro-channel

359 There exist a number of situations when the emergence of the wall slip phenomenon may turn quite problematic. The best
360 known example relates, perhaps, to the macro-rheological characterization of pasty materials where the presence of walls leads
361 to systematic errors particularly around the yield point. From a theoretical and numerical perspective the presence of wall
362 slip is equally troublesome as, to our best knowledge, there exists no fundamental theory that rigorously captures the scaling
363 behavior of the slip velocity at the wall and the choice of a slip law is often arbitrary. A direct way of eliminating the wall
364 slip which is commonly used during macro-rheological tests performed with pasty materials is to use mechanically rough solid
365 surfaces. Though effective in eliminating the wall slip, this solution comes at a price difficult to cope with during experiments
366 that require the in-situ visualization of the flow structure: the loss of the optical transparency. An alternative method relates to
367 "engineering" a special chemical treatment that facilitates the adhesion of the microstructural elements of the pasty material to a
368 solid wall without altering its optical transparency. For the case of a Carbopol gel, Metivier and co-workers proposed a chemical
369 reaction able to eliminate the slip along a smooth acrylic made wall, [1]. The authors of this study prove the effectiveness of
370 their method via macro-rheological tests performed with various gaps and indicate and equally emphasise its temporal stability
371 during 46 days. A detailed investigation of the physical mechanisms, responsible for the apparent macroscopic effectiveness of
372 this solution is, however, missing. After providing a detailed description of the chemical reaction, we focus in the following on
373 a detailed analysis of this solution via both macro-rheological tests and microfluidic experiments.

374 A. Chemical treatment of the micro-channel

375 The solution proposed by Metivier and her coworkers consists of depositing a thin layer of polyethylenimine *PEI* (Aldrich)
376 on the *Polymethyl methacrylate PMMA* surface. Low concentration of *PEI* solutions $C = 10^{-8} \text{ wt}\% - 2 \text{ wt}\%$ at neutral pH

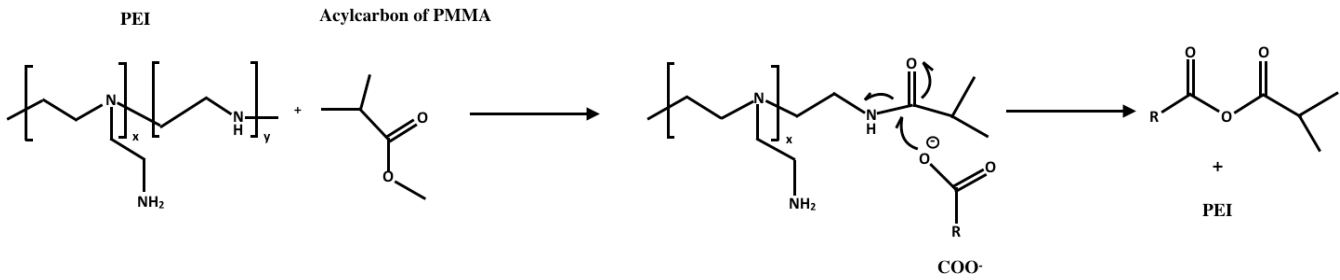


Figure 9. Chemical reaction leading to the attachment of the Carbopol gel on the PMMA surface.

377 have been prepared by dissolving the right amount of *PEI* in deionized water. The *PMMA* substrate was immersed into the *PEI*
 378 polymer solution during times ranging in between 60 *s* and 24 *h* and concluded that the final results is unchanged. Finally they
 379 have soaked the chemically treated substrate into double deionized water for 6 *h* in order to remove the excess (unreacted) of
 380 *PEI*.

381 The idea of the chemical treatment proposed by Metivier and her co-workers actually originates from a previous study by
 382 Kitagawa et al., [53]. Though apparently similar, the exact details of the procedure of Kitagawa and al. are actually quite differ-
 383 ent. The *PMMA* microchip was cleaned by damping it in methanol for 10 *mins* then rinsed in deionized water. A significantly
 384 higher concentration of *PEI* solution $C = 10 \text{ wt}\% - 20 \text{ wt}\%$ was used. To neutralize the *PEI* solutions, a borate buffer was
 385 equally added to the mixture. The neutralized solution was continuously circulated through the micro-channel for 2 *h*. The
 386 micro-channel was rinsed in deionized water for another 20 *mins*.

387 As only Metivier and her coworkers have studied the influence of the chemical treatment on the wall slip of Carbopol in Ref.
 388 [1], we have decided to follow their procedure in our study rather than that of Kitagawa et al. We used *PEI* solutions of 0.5 *wt%*
 389 concentration. We found that the *pH* is not neutral even for low concentration of *PEI*, $pH \approx 10.7$. The immersing time of our
 390 *PMMA* substrates was for 24 *h*.

391 According to Refs. [1, 53], the idea of these methods relies on a chemical reaction between the acylcarbon groups (ester
 392 groups) of the *PMMA* substrate with the secondary amino groups of *PEI* and a reaction between the COO^- groups of the
 393 Carbopol gel with the amino groups of *PEI* [1]. After a closer analysis of the chemical reaction in terms of the chemical affinity
 394 of the reactants, we conclude that the COO^- groups of the Carbopol gel actually bind to the amido groups as shown in Fig. 9.

395 These bonds lead to the attachment of Carbopol microgel particles to the *PMMA* substrate and the formation of a Carbopol
 396 layer essential in preventing the wall slip. We also note that, according to Fig. 9 some *PEI* molecules remain in the solution.

397 B. Assessment of wall slip behavior via macro-rheological measurements

398 First, we have assessed the effectiveness of the chemical treatment by means of macro-rheological tests. For this purpose,
 399 we have machined two identical acrylic blocks and treated only one of them according to the protocol described in Sec. III A
 400 while leaving the second chemically unaltered. The acrylic blocks have been used as bottom plates for macro-rheological tests.
 401 We note that the macro-rheological experiments with the chemically treated acrylic block were performed immediately after
 402 the treatment was completed thus avoiding any degradation of the chemical treatment in time. The temporal stability of the
 403 treatment will be discussed separately in Sec. III C. For all the experiments we have performed, glass paper was glued on the
 404 top plate (as described in Sec. I A 2). Thus, if any, the wall slip might solely occur on the bottom plate. The results of this
 405 comparative macro-rheological investigation are summarised in Fig. 10 which presents the dependence of the measured rate of
 406 deformation $\dot{\gamma}$ on the reduced applied stress τ/τ_y for several slip conditions on the bottom plate. When a chemically treated
 407 acrylic block is used as a bottom plate (the diamonds in Fig. 10), the macro-rheological measurements are practically identical
 408 to those performed in the absence of wall slip (when both plates are covered with glass paper, the circles in Fig. 10). On the other
 409 hand, the measurements performed with the untreated acrylic block as a bottom plate (the triangles in Fig. 10) deviate strongly
 410 from the measurements performed in the absence of slip particularly around the yield point, $\frac{\tau}{\tau_y} \approx 1$. To conclude this part, from
 411 a macro-rheological perspective, the wall slip effects are negligible when the acrylic surfaces of the rheometric geometry are
 412 chemically treated and the rheological tests are conducted immediately after the treatment.

413 This conclusion is in a general agreement with the main point made in Ref. [1]. To this end, however, the microscopic physical
 414 mechanism behind the apparent macroscopic effectiveness of this chemical treatment remains elusive. To gain further insights
 415 into this, we focus in the upcoming section on a detailed characterization of flows in chemically treated micro-channels and on
 416 their comparison with the flows in the presence of wall slip described in Sec. II.

417 C. Slip behavior in chemically treated micro-channels

418 To understand the impact of the chemical treatment on the microscopic flows we have performed measurements similar to
 419 those performed in the presence of wall slip with chemically treated micro-channels. The operating flow rates were chosen in
 420 the same range as in the case of the experiments described in II.

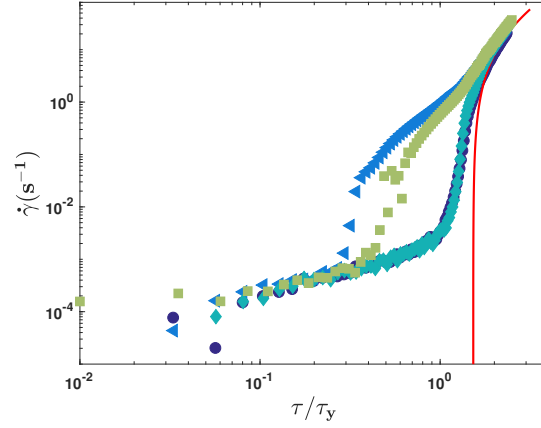


Figure 10. Macro-rheological measurements of the dependence of the rate of deformation $\dot{\gamma}$ on the reduced applied stress for various slip conditions on the bottom plate: circles - no slip (glass paper glued on the bottom plate), diamonds - chemically treated acrylic block used as a bottom plate immediately after the chemical treatment was completed, squares - chemically treated acrylic block used as a bottom plate one week after the chemical treatment, triangles - untreated acrylic block used as a bottom plate. The full line is a fit according to the Herschel-Bulkley model.

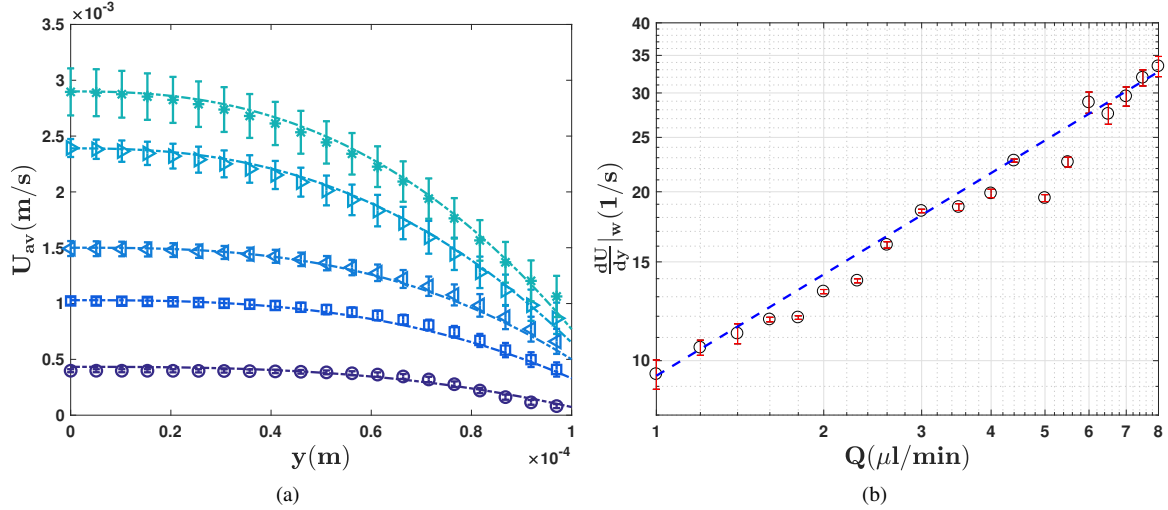


Figure 11. (a) Velocity profiles measured in the chemically treated micro-channel at various flow rates: circles- $Q = 1 \mu l/min$, squares- $Q = 2.6 \mu l/min$, left triangles- $Q = 4 \mu l/min$, right triangles- $Q = 6.5 \mu l/min$, stars- $Q = 8 \mu l/min$. The dash dotted lines are fitting functions according to analytical solution of the Poiseuille flow of a power law fluid given by Eq. 2. (b) Dependence of the wall velocity gradients measured in the chemically treated micro-channel on the applied flow rate Q . The dashed line (---) is a guide for the eye, $\frac{dU}{dy}|_w \propto Q^{0.6}$.

421 Velocity profiles measured in the chemically treated micro-channel for several flow rates are presented in fig. 11(a). Unlike
 422 in the case of the untreated channels, we no longer observe neither a full plug flow regime as illustrated in Fig. 5(a) nor an
 423 intermediate regime as in Fig. 5(b). For each flow rate Q , the velocity profiles are qualitatively similar to those observed in the
 424 yielded regime illustrated in Fig. 5(c) and can be fitted by the analytical solution for the Poiseuille flow of a power law fluid
 425 given by Eq. 2.

426 A direct consequence of the chemical treatment relates to larger velocity gradients in the proximity of the wall as well as to
 427 smaller slip velocities as visible in Fig. 11(b). However, these measurements clearly indicate the slip at the wall is not completely
 428 removed by the chemical treatment but only inhibited. Thus, at a microscopic scale, the effectiveness of the chemical treatment
 429 is only partial.

430 The comparison of the dependencies of the plug velocity U_p , slip velocity U_s and the wall shear rates $\frac{dU}{dy}|_w$ on the driving
 431 flow rate Q measured in chemically treated and untreated channels is shown in Fig. 12. As already noted, for the case of the
 432 chemically treated channel the slip velocity is smaller than in the case of the untreated channel, Fig. 12(b). Consequently, the
 433 plug velocity is systematically larger in the treated channel.

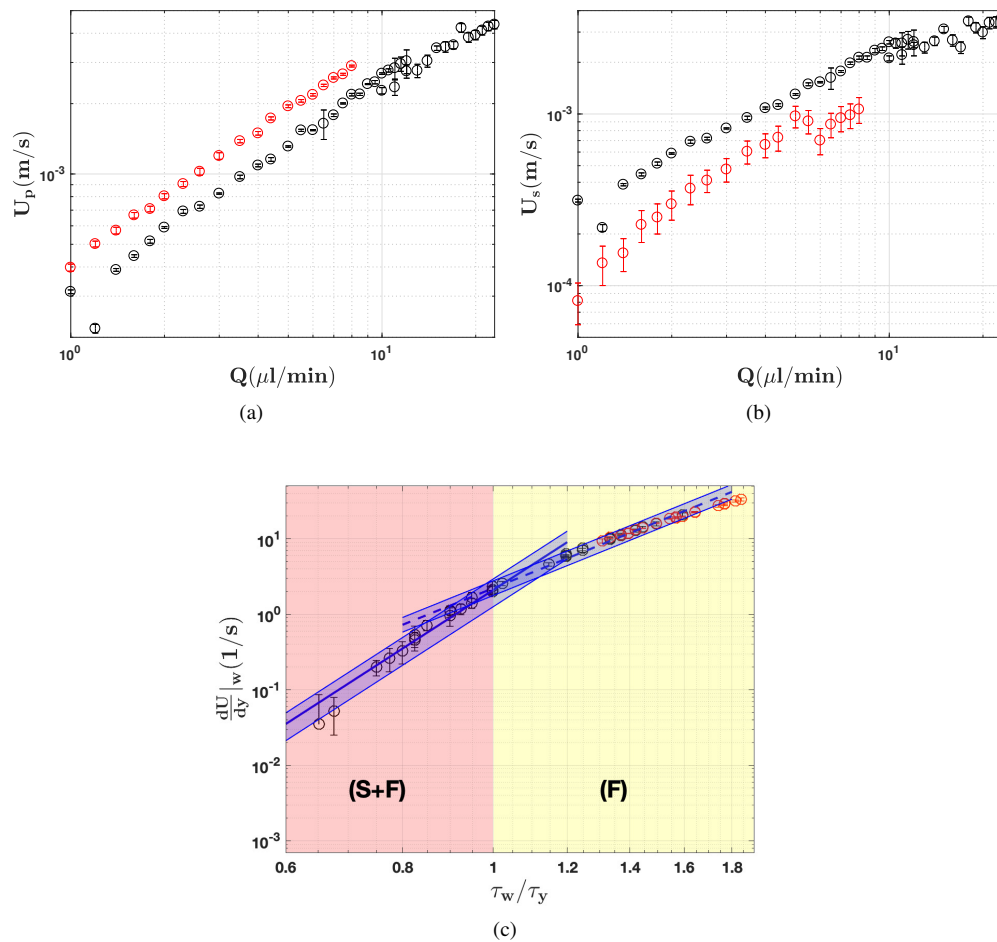


Figure 12. (a) Dependence of the slip velocity U_s on the volumetric flow rate Q . (b) Dependence of the plug velocity U_p on the volumetric flow rate Q . (c) dependence of the wall velocity gradient $\frac{dU}{dy}|_w$ vs. wall shear stress τ_w . Black/red circles correspond to the treated/untreated *PMMAmicro* – channel. The blue shaded regions overlapped onto the fit functions represent the error bounds of the power law fits.

434 The dependence of the wall velocity gradients on the wall shear stress measured in the chemically treated channel is fully
 435 consistent with the measurements performed with the untreated channel in the third flow regime, 12(c). This reinforces the state-
 436 ment that in the chemically treated channel a single flow regime is observed corresponding to the largest flow rates investigated
 437 with the untreated channel.

438 To gain further insights into the physical mechanism by which the chemical treatment affects the slip behavior we turn
 439 our attention to the direct visualisation of the flow in both untreated and chemically treated channels at the same flow rate
 440 $Q = 1 \mu\text{l}/\text{min}$. Two distinct methods of flow visualisation have been employed. First, we have performed direct imaging of
 441 the streaks of the micro-PIV seeding particles by overexposing the images prior to acquisition. This kind of visualisation offers
 442 primary insights into the structure of the microscopic flow. Second, we display the corresponding microscopic flow fields.

443 The flow in the untreated channel is described in Fig. 13. As one would expect for the case of a steady and laminar flow, the
 444 streak lines are rectilinear and parallel to the walls of the micro-channel, Fig. 13(a). Consequently, the velocity field exhibits no
 446 component in the direction transversal to the flow, Fig. 13(b).

447 The flow in the chemically treated micro-channel is illustrated in Fig. 14. The image of the streaks of the seeding particles
 448 reveal the presence of rigid blobs of Carbopol unevenly attached to the walls of the micro-channel (the regions highlighted by
 449 the yellow ellipses in Fig. 14(a).) By monitoring the streak line behavior at various positions downstream we have observed
 450 no regularity of their distribution along the channel walls and thus we have concluded that their appearance is rather random.
 451 We attribute this apparent randomness to the polydispersity of the Carbopol microstructure which has been demonstrated exper-
 452 imentally, [41, 54]. The presence of these solid blobs attached to the micro-channel walls induces a secondary flow, Fig. 14(b).
 453 Whereas in a macroscopic geometry this effect might be of little or no importance, in a micro-channel with a size of the same
 454 order of magnitude as the average size of the gel particles this effect can no longer be ignored.

455 A second issue related to the overall effectiveness of this chemical treatment is its temporal stability. To address this issue we

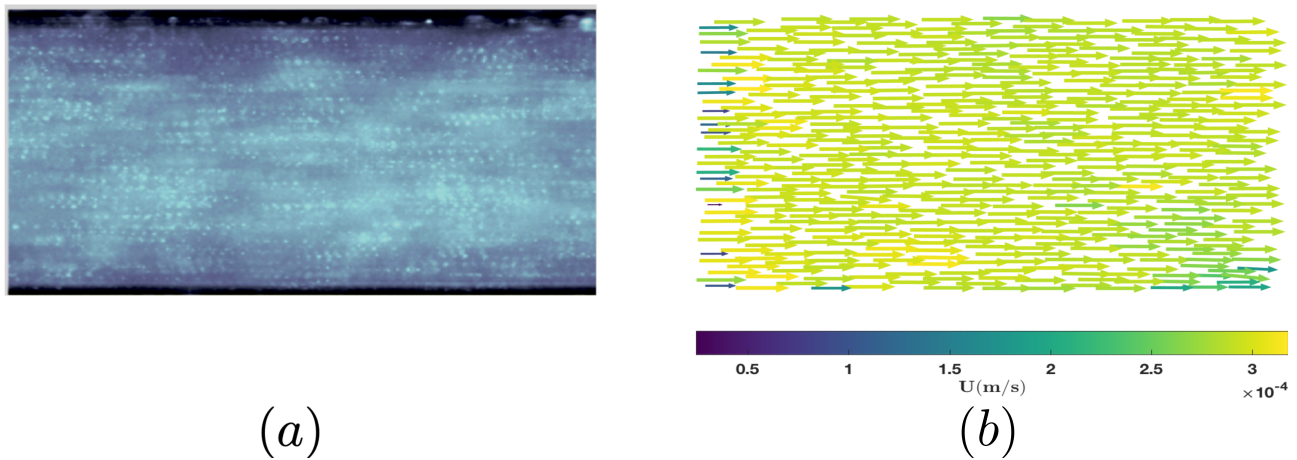


Figure 13. (a) Streak imaging of the flow in the untreated micro-channel. (b) Velocity field measured in the chemically untreated channel. The flow rate was $Q = 1 \mu\text{l}/\text{min}$.

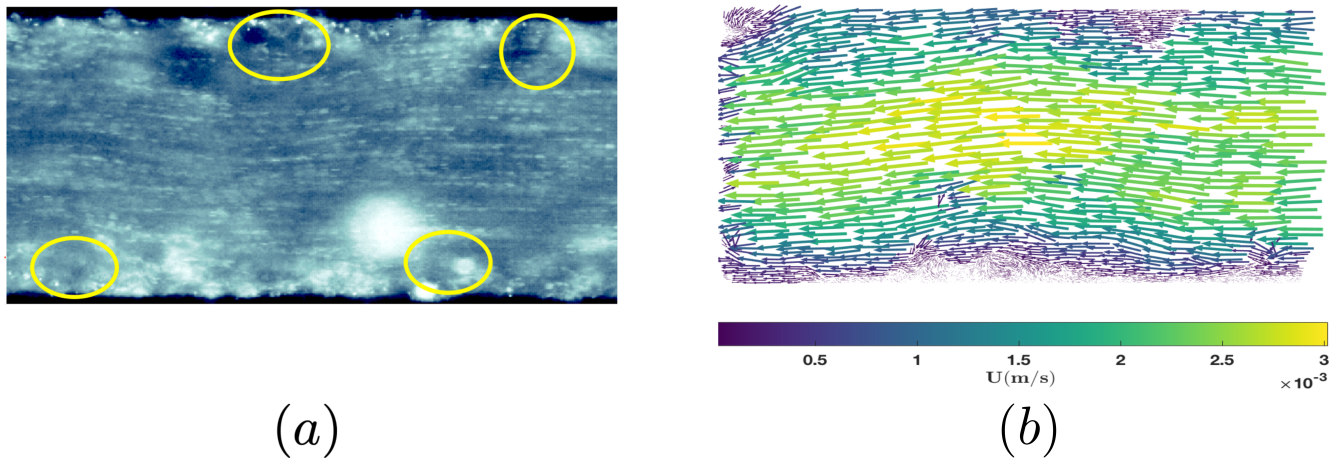


Figure 14. (a) Streak imaging of the flow in the chemically treated micro-channel. The yellow ellipses highlight blobs of the gel rigidly attached to the walls. (b) Velocity field measured in the chemically treated channel. The flow rate was $Q = 1 \mu\text{l}/\text{min}$.

456 have performed macro-rheological tests similar to those presented in Fig. 10 after keeping the chemically treated acrylic blocks
 457 in a beaker filled with deionized water for one week in conditions of gentle stirring with a magnetic stirring rod. The result was
 458 that the slip behavior illustrated in Fig. 10 was restored which indicated that the effectiveness of the treatment was basically lost
 459 - the squares in Fig. 10.

460 IV. Summary of conclusions, outlook

461 An experimental investigation of the wall slip phenomenon during a steady micro-flow of a Carbopol gel was carried out in
 462 this study. By means of Digital Particle Image Velocimetry, accurate measurements of the flow fields have been performed in a
 463 wide range of flow rates. Depending on the magnitude of the flow rate, three distinct flow regimes are observed. At low driving
 464 flow rates, a full plug flow regime is observed, Fig. 5(a). The full plug flow regime may be understood in terms of a solid body of
 465 un-yielded gel sliding over a thin layer of depleted solvent expelled from the spongy Carbopol structural units in the vicinity
 466 of the solid walls. As the flow rate is gradually increased, the Carbopol gel is partially yielded in the proximity of the channel
 467 walls but a central un-yielded plug may still be observed around the centre-line of the micro-channel, Fig. 5(b). As the flow rate
 468 is increased even further, the Carbopol gel is fully yielded across the entire width of the channel, Fig. 5(c).

469 As the flow rate is increased past the full plug regime, the plug length W_p decreases monotonically from a value equal to half
 470 channel width $W/2$ to zero, Fig. 6. The scaling behavior of the wall velocity gradients $\frac{dU}{dy}|_w$ with the flow rate is illustrated in
 471 Fig. 7(a). Within the partially yielded regime, $\frac{dU}{dy}|_w \propto Q^2$ whereas within the fully yielded regime $\frac{dU}{dy}|_w \propto Q^3$.

472 Measurements of the velocity profiles allow one to obtain the wall velocity gradients and slip velocities by extrapolating the
 473 velocity profiles at the channel walls. We use the dependence between the stress and the rate of shear obtained via classical

rotational rheometry and we relate the measured wall velocity gradients to the wall stresses in order to obtain experimentally the scaling laws for the wall slip phenomenon.

As compared to a number of previous studies that inferred the wall velocity gradients and the wall shear stresses directly from the driving pressure drops and flow rates [16, 20, 22], this procedure has the important advantage of making absolutely no assumption on either the flow structure or the rheological behavior of the material. The scaling behavior of the wall velocity gradients with respect to the wall shear stresses is illustrated in Fig. 7(b). Within the partially yielded regime, the wall velocity gradients scale as $\frac{dU}{dy}|_w \propto \tau_w^{7.99}$ whereas in the fully yielded regime as $\frac{dU}{dy}|_w \propto \tau_w^{4.8}$.

Two distinct scaling laws of the slip velocity U_s with the wall shear stress τ_w are observed when the flow rates are increased past the full plug regime. Within the partially yielded flow regime, a power law scaling of the slip velocity with the wall shear stress is observed, $U_s \propto \tau_w^{3.5}$, the full line in Fig. 8(a). Within the fully yielded flow regime, the scaling becomes linear, $U_s \propto \tau_w$, the dashed line Fig. 8(a). For both the partially yielded and fully yielded regimes, a power law scaling of the slip velocity with the wall velocity gradients $\frac{dU}{dy}|_w$ is observed, 8(b).

The physical reasons behind the emergence of a power law scaling for the physical quantities relevant in describing the wall slip behaviour remain elusive. A power law scaling is often a signature of hierarchical organisation in a complex system, which in this case is the microstructure of the Carbopol gel during yielding. The implicit hypothesis underpinning our work is the phenomenon of wall slip is intrinsically dependent on the fluid microstructural changes during yielding. Since it was demonstrated that the yielding of a yield stress material may be understood as a bifurcation phenomenon (or a phase transition) [26, 38], we may suggest that the wall slip exhibits a similar behavior hence a similar mathematical structure, which justifies the use of a power law to fit the experimental data. Unfortunately, the constraints dictated by the physical system under consideration allow us to validate the power law behaviour only over a limited range of the parameter values, which is an issue we are fully aware of.

Through the last part of the paper, we have investigated the effectiveness of a chemical treatment proposed by Métivier and coworkers in ref. [1] in removing the wall slip effects. Whereas the treatment is indeed able to remove the wall slip effects during macro-rheological tests, Fig. 10, its effectiveness at a microscopic scale is somewhat more limited. First, although the treatment is able to inhibit the wall slip effects (the slip velocities are smaller and the wall velocity gradients significantly larger), it does not completely remove them, Fig. 11(a). A second drawback of the chemical treatment relates to the emergence of secondary flow due to the presence of solid blobs attached to the walls of the micro-channel at positions randomly distributed downstream, Fig. 14. Third, the temporal stability of this treatment is limited: after a week, the effects of the treatment vanished and the macroscopic slip behavior was fully restored, the squares in Fig. 10.

The results presented in this study clearly call for both experimental and theoretical studies along several lines. On the experimental side, future studies that could capture the evolution of the micro-structure of the yield material with the flow would help clarifying the generally accepted (but, to our best knowledge, not demonstrated experimentally) picture of a thin depleted layer of solvent in the vicinity of the solid surface. This is a rather difficult task as it requires the development of a chemical reaction able to graft a low molar mass fluorescent compound on the micro-structural units of the gel without altering its yield stress behavior. An important step in this direction has already been made by designing a chemical reaction able to covalently stain the Carbopol structural units with Rhodamine which allows one to visualise the dynamics of the solid micro-structural during microscopic flows, [44].

On a theoretical line, in order to understand the physical mechanisms of the wall slip, one needs to develop a theoretical physico-chemical framework able to confirm the formation of a depleted layer of the solvent near the wall which in turn would allow one to predict analytical laws for the scaling of the slip velocity with the wall shear stresses. Last, such physical picture of the wall slip needs to be later be incorporated in a novel constitutive law able to fully describe the flow in the presence of slip.

V. Acknowledgements

We acknowledge the Agence Nationale de la Recherche (ANR) for the financial support via project NaiMYS (ANR-16-CE06-0003).

V.B. gratefully acknowledges a visiting fellowship from Polytech Nantes.

E.Y. and T.B. are deeply indebted to Prof. Georgios C. Georgiou for valuable discussions on flows of yield stress fluids in the presence wall slip.

-
- [1] C. Metivier, Y. Rharbi, A. Magnin, and A. Bou Abboud, Stick-slip control of the carbopol microgels on polymethyl methacrylate transparent smooth walls, *Soft Matter* **8**, 7365 (2012).
 - [2] M. Cloître, *Advance in Polymer Science 236, High Solid Dispersions* (Springer-Verlag Berlin Heidelberg, Berlin, 2010).
 - [3] M. Cloître and T. Bonnecaze, Roger, A review of wall slip in high solid suspensions, *Rheologica Acta* **56**, 283 (2017).
 - [4] P. Tabeling, Phénomènes de glissement à l'interface liquide–solide, *Comptes Rendus Physique* **5**, 531 (2004), microfluidics.
 - [5] J.-H. J. Cho, B. M. Law, and F. m. c. Rieutord, Dipole-dependent slip of newtonian liquids at smooth solid hydrophobic surfaces, *Phys. Rev. Lett.* **92**, 166102 (2004).

- [6] P. Panaseti, A.-L. Vayssade, G. C. Georgiou, and M. Cloitre, Confined viscoplastic flows with heterogeneous wall slip, *Rheologica Acta* **56**, 539 (2017).
- [7] Y. Damianou, G. Kaoullas, and G. C. Georgiou, Cessation of viscoplastic poiseuille flow in a square duct with wall slip, *Journal of Non-Newtonian Fluid Mechanics* **233**, 13 (2016), papers presented at the Rheology Symposium in honor of Prof. R. I. Tanner on the occasion of his 82nd birthday, in Vathi, Samos, Greece.
- [8] S. P. Meeker, R. T. Bonnecaze, and M. Cloitre, Slip and flow in soft particle pastes, *Phys. Rev. Lett.* **92**, 198302 (2004).
- [9] J. R. Seth, M. Cloitre, and R. T. Bonnecaze, Influence of short-range forces on wall-slip in microgel pastes, *Journal of Rheology* **52**, 1241 (2008), <https://doi.org/10.1122/1.2963135>.
- [10] P. Ballesta, R. Besseling, L. Isa, G. Petekidis, and W. C. K. Poon, Slip and flow of hard-sphere colloidal glasses, *Phys. Rev. Lett.* **101**, 258301 (2008).
- [11] P. Ballesta, G. Petekidis, L. Isa, W. C. K. Poon, and R. Besseling, Wall slip and flow of concentrated hard-sphere colloidal suspensions, *Journal of Rheology* **56**, 1005 (2012), <https://doi.org/10.1122/1.4719775>.
- [12] X. Zhang, E. Lorenceau, P. Basset, T. Bourouina, F. Rouyer, J. Goyon, and P. Coussot, Wall slip of soft-jammed systems: A generic simple shear process, *Phys. Rev. Lett.* **119**, 208004 (2017).
- [13] T. Divoux, V. Lapeyre, V. Ravaine, and S. Manneville, Wall slip across the jamming transition of soft thermoresponsive particles, *Phys. Rev. E* **92**, 060301 (2015).
- [14] Germain, D. and Le Merrer, M., Bubbles slipping along a crenelated wall, *EPL* **115**, 64005 (2016).
- [15] A. Poumaere, M. Moyers-Gonzalez, C. Castelain, and T. Burghelaea, Unsteady laminar flows of a carbopol gel in the presence of wall slip, *Journal of Non-Newtonian Fluid Mechanics* **205**, 28 (2014).
- [16] J. Pérez-González, J. J. López-Durán, B. M. Marín-Santibáñez, and F. Rodríguez-González, Rheo-piv of a yield-stress fluid in a capillary with slip at the wall, *Rheologica Acta* **51**, 937 (2012).
- [17] D. M. Kalyon, Apparent slip and viscoplasticity of concentrated suspensions, *Journal of Rheology* **49**, 621 (2005), <https://doi.org/10.1122/1.1879043>.
- [18] V. Bertola, F. Bertrand, H. Tabuteau, D. Bonn, and P. Coussot, Wall slip and yielding in pasty materials, *Journal of Rheology* **47**, 1211 (2003), <https://doi.org/10.1122/1.1595098>.
- [19] Y. Liu, D. Lorusso, D. W. Holdsworth, T. L. Poeping, and J. R. de Bruyn, Effect of confinement on the rheology of a yield-stress fluid, *Journal of Non-Newtonian Fluid Mechanics* **261**, 25 (2018).
- [20] B. Geraud, L. Bocquet, and C. Barentin, Confined flows of a polymer microgel, *The European Physical Journal E* **36**, 30 (2013).
- [21] A.-L. Vayssade, C. Lee, E. Terriac, F. Monti, M. Cloitre, and P. Tabeling, Dynamical role of slip heterogeneities in confined flows, *Phys. Rev. E* **89**, 052309 (2014).
- [22] J. Péméja, B. Geraud, C. Barentin, and M. Le Merrer, Wall slip regimes in jammed suspensions of soft microgels, *Phys. Rev. Fluids* **4**, 033301 (2019).
- [23] V. Bertola, Wicking with a yield stress fluid, *Journal of Physics Condensed Matter* **21**, 10.1088/0953-8984/21/3/035107 (2009).
- [24] G. German and V. Bertola, The spreading behaviour of capillary driven yield-stress drops, *Colloids and Surfaces A: Physicochemical and Engineering Aspects* **366**, 18 (2010).
- [25] G. German and V. Bertola, Formation of viscoplastic drops by capillary breakup, *Physics of Fluids* **22**, 1 (2010).
- [26] T. Burghelaea and V. Bertola, *Transport phenomena in complex fluids* (Springer International Publishing, 2019).
- [27] E. Kaliviotis, J. M. Sherwood, and S. Balabani, Local viscosity distribution in bifurcating microfluidic blood flows, *Physics of Fluids* **30**, 030706 (2018), <https://doi.org/10.1063/1.5011373>.
- [28] A.-L. Vayssade, *Flows of Herschel-Bulkley fluids in confined environments : applications to the cementing of oil wells*, Ph.D. thesis, l'Université Pierre et Marie Curie.
- [29] J. R. Seth, C. Locatelli-Champagne, F. Monti, R. T. Bonnecaze, and M. Cloitre, How do soft particle glasses yield and flow near solid surfaces?, *Soft Matter* **8**, 140 (2012).
- [30] V. Mansard, L. Bocquet, and A. Colin, Boundary conditions for soft glassy flows: slippage and surface fluidization, *Soft Matter* **10**, 6984 (2014).
- [31] S. G. Hatzikiriakos, Slip mechanisms in complex fluid flows, *Soft Matter* **11**, 7851 (2015).
- [32] S. G. Hatzikiriakos, Wall slip of molten polymers, *Progress in Polymer Science* **37**, 624 (2012), topical Issue on Polymer Physics.
- [33] S. Curran, R. Hayes, A. Afacan, M. Williams, and P. Tanguy, Properties of carbopol solutions as models for yield-stress fluids, *Journal of Food Science* **67**, 176 (2002), <https://onlinelibrary.wiley.com/doi/pdf/10.1111/j.1365-2621.2002.tb11379.x>.
- [34] G. Ovarlez, S. Cohen-Addad, K. Krishan, J. Goyon, and P. Coussot, On the existence of a simple yield stress fluid behavior, *Journal of Non-Newtonian Fluid Mechanics* **193**, 68 (2013), viscoplastic Fluids: From Theory to Application.
- [35] J. Piau, Carbopol gels: Elastoviscoplastic and slippery glasses made of individual swollen sponges: Meso- and macroscopic properties, constitutive equations and scaling laws, *Journal of Non-Newtonian Fluid Mechanics* **144**, 1 (2007).
- [36] T. Divoux, D. Tamarii, C. Barentin, and S. Manneville, Transient shear banding in a simple yield stress fluid, <http://arxiv.org/abs/1003.0161v1> (2009).
- [37] A. M. V. Putz and T. I. Burghelaea, The solid-fluid transition in a yield stress shear thinning physical gel, *Rheol Acta* **48**, 673 (2009).
- [38] T. Burghelaea, M. Moyers-Gonzalez, and R. Sainudiin, A nonlinear dynamical system approach for the yielding behaviour of a viscoplastic material, *Soft Matter* **13**, 2024 (2017).
- [39] E. Weber, M. Moyers-Gonzalez, and T. I. Burghelaea, Thermorheological properties of a carbopol gel under shear, *Journal of Non-Newtonian Fluid Mechanics* **183-184**, 14 (2012).
- [40] M. M. Gonzalez, T. Burghelaea, and J. Mak, Linear stability analysis for plane-poiseuille flow of an elastoviscoplastic fluid with internal microstructure for large reynolds numbers, *Journal of Non-Newtonian Fluid Mechanics* **166**, 515 (2011).
- [41] F. K. Oppong and J. R. de Bruyn, Diffusion of microscopic tracer particles in a yield-stress fluid, *J. Non-Newtonian Fluid Mech.* **142**, 104 (2007).

- 592 [42] I. Gutowski, D. Lee, J. de Bruyn, and B. Frisken, Scaling and mesostructure of carbopol dispersions, *Rheologica Acta* , 1 (2012),
593 10.1007/s00397-011-0614-6.
- 594 [43] R. Sainudiin, M. Moyers-Gonzalez, and T. Burghelea, A microscopic gibbs field model for the macroscopic yielding behaviour of a
595 viscoplastic fluid, *Soft Matter* **11** (27), 5531 (2015).
- 596 [44] E. Younes, M. Himl, Z. Sary, V. Bertola, and T. Burghelea, On the elusive nature of carbopol gels: “model”, weakly thixotropic, or
597 time-dependent viscoplastic materials?, *Journal of Non-Newtonian Fluid Mechanics* **281**, 104315 (2020).
- 598 [45] T. Thorsen, S. J. Maerkl, and S. R. Quake, Microfluidic large-scale integration, *Science* **298**, 580 (2002),
599 <http://science.sciencemag.org/content/298/5593/580.full.pdf>.
- 600 [46] F. Scarano and M. L. Rhiethmuller, Advances in iterative multigrid piv image processing, *Exp. Fluids* **29** (2001).
- 601 [47] M. Raffel, C. E. Willert, S. T. Wereley, and J. Kompenhans, *Particle Image Velocimetry: A Practical Guide (Experimental Fluid Mechan-*
602 *ics)* (Springer; 2nd edition, September 2007).
- 603 [48] H. A. Barnes, A review of the slip (wall depletion) of polymer solutions, emulsions and particle suspensions in viscometers: its cause,
604 character, and cure, *Journal of Non-Newtonian Fluid Mechanics* **56**, 221 (1995).
- 605 [49] L. Ferrás, J. Nóbrega, and F. Pinho, Analytical solutions for newtonian and inelastic non-newtonian flows with wall slip, *Journal of*
606 *Non-Newtonian Fluid Mechanics* **175-176**, 76 (2012).
- 607 [50] Y. Damianou, M. Philippou, G. Kaoullas, and G. C. Georgiou, Cessation of viscoplastic poiseuille flow with wall slip, *Journal of Non-*
608 *Newtonian Fluid Mechanics* **203**, 24 (2014).
- 609 [51] S. P. Meeker, R. T. Bonnecaze, and M. Cloitre, Slip and flow in pastes of soft particles: Direct observation and rheology, *Journal of*
610 *Rheology* **48**, 1295 (2004).
- 611 [52] T. Jiang, A. Young, and A. Metzner, The rheological characterization of hpg gels: Measurement of slip velocities in capillary tubes,
612 *Rheologica Acta* **25**, 397 (1986).
- 613 [53] F. Kitagawa, K. Kubota, K. Sueyoshi, and K. Otsuka, One-step immobilization of cationic polymer onto a poly(methyl methacrylate)
614 microchip for high-performance electrophoretic analysis of proteins, *Science and Technology of Advanced Materials* **7**, 558 (2006),
615 <https://doi.org/10.1016/j.stam.2006.02.021>.
- 616 [54] F. K. Oppong, L. Rubatat, B. J. Frisken, A. E. Bailey, and J. R. de Bruyn, Microrheology and structure of a yield-stress polymer gel,
617 *Phys. Rev. E* **73**, 041405 (2006).